Efficient hybrid density functional calculations for solids with a local basis set

Giacomo Ambrogio, Jacques K. Desmarais,* and Alessandro Erba†
Dipartimento di Chimica, Università di Torino, via Giuria 5, 10125 Torino, Italy

(Received 12 February 2026; accepted 26 June 2026; published 20 July 2026)

The applicability of hybrid density functional approximations (DFAs) in the solid state is still largely hindered by a high computational cost in the evaluation of the exact exchange series. We review formal and computational aspects of a direct space approach to the evaluation of exact exchange in periodic systems with local, atom-centered, Gaussian-type basis functions. We discuss an efficient prescreening strategy in terms of the localized basis to either truncate the series via overlap-based criteria or partition it into distinct regions where the integrals can be computed exactly or approximately via a bipolar expansion of the Coulomb operator. The inclusion of exact exchange in hybrid DFAs largely corrects for the self-interaction error, ensures a better description of electron localization, and thus proves crucial to the characterization of defects, strongly correlated materials, band gaps in semiconductors, as well as to an effective treatment of spin-orbit and electron-phonon couplings. Three test systems are considered, which have been selected as representative of different electronic regimes: (i) bulk hematite, α-Fe_2O_3, in its insulating, antiferromagnetic configuration; (ii) semiconducting single-layer WSe_2 (with inclusion of spin-orbit coupling); and (iii) bulk EuO in its metallic ferromagnetic phase at a pressure of 20 GPa. The strategy is assessed on various electronic properties (energy, band gap, spin magnetic moment, Rashba splitting) and is documented to yield calculations with hybrid DFAs with a relative cost of just 3–6 times that of standard (semi)local DFAs.

DOI: 10.1103/wgd9-321t

I. INTRODUCTION

Density functional theory (DFT) [1] is the most widely applied method in computational materials science. In "global" hybrid approximations [2], exchange and correlation (xc) potential includes a fraction α of exact, nonlocal, Fock exchange v_{Fock} according to

$$v_{\text{xc}}([n];\mathbf{r},\mathbf{r}') = \alpha v_{\text{Fock}}(\mathbf{r},\mathbf{r}') + (1-\alpha)v_{\text{x}}([n];\mathbf{r}) + v_{\text{c}}([n];\mathbf{r}), \tag{1}$$

where v_{x} and v_{c} are semilocal density functional approximations, typically of local density approximation or generalized-gradient approximation (GGA) type. Many popular global hybrid functionals are defined in terms of a fixed (thus system-independent) value for α (0.2 in B3LYP and B3PW91, 0.25 in PBE0, 0.16 in B1WC, just to name a few) [2–6]. Alternatively, a system-specific value for α can be defined in terms of its electronic screening, with a popular prescription being $\alpha \propto \epsilon_\infty^{-1}$, where ϵ_∞ is the static electronic dielectric constant of the material [7–15]. In range-separated hybrid density functional approximations (DFAs), the Coulomb operator is split into short- and long-range terms that are treated separately [16–18]. A popular approach for calculations on extended systems consists in including exact nonlocal Fock exchange only at short range (more on this in Sec. II B 3), as in Heyd-Scuseria-Ernzerhof (HSE) family of DFAs [19,20].

Nowadays, it is widely accepted that the presence of a fraction of exact Fock exchange in hybrid DFAs largely corrects for the self-interaction error (SIE) [21], leading to an overall higher accuracy in the prediction of many solid-state properties [22–25]. This proves particularly crucial in the fields of electronics and spintronics, with the calculation of band gaps in semiconductors and a variety of aspects of electron spin and magnetism [26–30].

And yet, hybrid DFAs are still not as widely applied for solids as they are for finite molecular systems due to a high computational cost [31]. While the range-separation strategy has certainly helped to partially solve the problem [20,25], the use of localized basis sets in solids ensures maximal efficiency [31–34]. In this paper, we review an all-electron direct space approach to the evaluation of Fock exchange in periodic systems with atom-centered, Gaussian-type basis functions. Application to hybrid DFAs—both in their global and range-separated versions—is discussed, and their efficiency assessed with respect to the GGA. Three test systems are considered, which have been selected as representative of different electronic regimes: (i) bulk hematite, α-Fe_2O_3, in its insulating, antiferromagnetic configuration; (ii) semiconducting single-layer WSe_2 (with inclusion of spin-orbit coupling); and (iii) bulk EuO in its metallic ferromagnetic phase at a pressure of 20 GPa.

II. FORMAL ASPECTS AND IMPLEMENTATION

A. Direct space LCAO approach

We work within a linear combination of atomic orbitals (LCAO) approach. For ease of notation, in the following, we present the equations for the spin-restricted case. One-electron

*Contact author: jacqueskontak.desmarais@unito.it
†Contact author: alessandro.erba@unito.it

 ©2026 American Physical Society

orbitals $\psi_i(\mathbf{r};\mathbf{k})$ are built as linear combination of atomic functions $\phi_\mu(\mathbf{r};\mathbf{k})$ via coefficients $a^{\mathbf{k}}_{\mu,i}$ and $\phi_\mu(\mathbf{r};\mathbf{k})$, which are written in terms of atomic orbitals (AOs) $\chi_\mu(\mathbf{r})$,

$$\psi_i(\mathbf{r};\mathbf{k}) = \sum_{\mu=1}^{N} a^{\mathbf{k}}_{\mu,i}\phi_\mu(\mathbf{r};\mathbf{k}), \tag{2a}$$

$$\phi_\mu(\mathbf{r};\mathbf{k}) = \sum_{\mathbf{g}} \chi^{\mathbf{g}}_\mu(\mathbf{r})e^{i\mathbf{k}\cdot\mathbf{g}}. \tag{2b}$$

Here, $\mathbf{r}$ are the coordinates of an electron, $\mathbf{k}$ denotes a sampling point in reciprocal space, and the summation in Eq. (2b) is extended to the set of all lattice vectors $\mathbf{g}$. In Eq. (2b), we have introduced the shorthand notation $\chi^{\mathbf{g}}_\mu(\mathbf{r}) = \chi_\mu(\mathbf{r} - \mathbf{c}_\mu - \mathbf{g})$, where $\mathbf{c}_\mu$ is the position in the reference cell on which χ_μ is centered. The AOs are, in turn, expressed as a linear combination of real spherical Gaussian-type functions (GTFs),

$$\chi^{\mathbf{g}}_\mu(\mathbf{r}) = \sum_{j=1}^{n_\lambda} d^\lambda_j\, G^m_{l,n}\big(\alpha^\lambda_j;\mathbf{r} - \mathbf{c}_\mu - \mathbf{g}\big), \tag{3}$$

where d^λ_j and α^λ_j are fixed coefficients and exponents of the shell λ containing μ. The grouping into shells ensures that AOs with the same quantum numbers n and l share the same d coefficients and α exponents. Many quantities are thus shell dependent rather than AO dependent, which reduces the size of matrices [35]. The $G^m_{l,n}(\alpha,\mathbf{r}) = X^m_{l,n}(\mathbf{r})\exp[-\alpha\mathbf{r}^2]$ functions in Eq. (3) are written as a product of a Gaussian function times a normalized real-solid-spherical harmonic $X^m_{l,n}$.

It proves convenient to introduce a single, normalized, s-type (i.e., with $l = 0$) GTF G_λ with the smallest exponent of each shell λ. These so-called *adjoined* Gaussians will be extensively used in the definition of overlap-based criteria for the partitioning and truncation of several direct lattice summations (see below).

Because of the orthogonality of one-electron orbitals associated to different $\mathbf{k}$ points, the expansion coefficients $a^{\mathbf{k}}_{\mu,i}$ in the atomic basis in Eq. (2a) are calculated by solving the following matrix equation for each point within the first Brillouin zone (FBZ):

$$\mathbf{H}^{\mathbf{k}}\mathbf{A}^{\mathbf{k}} = \mathbf{S}^{\mathbf{k}}\mathbf{A}^{\mathbf{k}}\mathbf{E}^{\mathbf{k}}, \tag{4}$$

where $\mathbf{E}^{\mathbf{k}}$ is the diagonal matrix of one-electron energy eigenvalues $\varepsilon^{\mathbf{k}}_i$, and $\mathbf{S}^{\mathbf{k}}$ and $\mathbf{H}^{\mathbf{k}}$ are the overlap and Kohn-Sham Hamiltonian matrices, that we compute from the corresponding matrices in the AO basis through a Fourier transform,

$$S^{\mathbf{k}}_{\mu\nu} = \sum_{\mathbf{g}} S^{\mathbf{g}}_{\mu\nu}e^{i\mathbf{k}\cdot\mathbf{g}} \quad \text{with} \quad S^{\mathbf{g}}_{\mu\nu} \equiv \langle\mu\mathbf{0}|\nu\mathbf{g}\rangle, \tag{5}$$

$$H^{\mathbf{k}}_{\mu\nu} = \sum_{\mathbf{g}} H^{\mathbf{g}}_{\mu\nu}e^{i\mathbf{k}\cdot\mathbf{g}} \quad \text{with} \quad H^{\mathbf{g}}_{\mu\nu} \equiv \langle\mu\mathbf{0}|\hat{H}|\nu\mathbf{g}\rangle. \tag{6}$$

The integrals $\langle\mu\mathbf{0}|\nu\mathbf{g}\rangle$ and $\langle\mu\mathbf{0}|\hat{H}|\nu\mathbf{g}\rangle$ are computed analytically using standard methods [35–37]. In the AO basis, the function in the bra can be restricted within the reference cell by exploiting translational invariance. The Hamiltonian matrix can be separated into one-electron and two-electron terms $\mathbf{H}^{\mathbf{g}} = \mathbf{M}^{\mathbf{g}} + \mathbf{B}^{\mathbf{g}}$,

$$\mathbf{M}^{\mathbf{g}} = \mathbf{T}^{\mathbf{g}} + \mathbf{Z}^{\mathbf{g}} + \mathbf{U}^{\mathbf{g}}_{\mathrm{RECP}}, \tag{7}$$

$$\mathbf{B}^{\mathbf{g}} = \mathbf{C}^{\mathbf{g}} + \mathbf{V}^{\mathbf{g}}_{\mathrm{xc}}. \tag{8}$$

One-electron terms are the electronic kinetic, electron-nuclei interaction, and relativistic effective core potential (RECP) contributions. For all-electron calculations, $\mathbf{U}^{\mathbf{g}}_{\mathrm{RECP}} = \mathbf{0}$ in Eq. (7). Two-electron terms are the usual Coulomb and exchange-correlation potentials. Let us focus on the two-electron contributions. In the AO basis, the matrix elements of the Coulomb term read

$$C^{\mathbf{g}}_{\mu\nu} = \sum_{\sigma\rho}\sum_{\mathbf{q}} P^{\mathbf{q}}_{\sigma\rho}\sum_{\mathbf{s}}\big(\chi^{\mathbf{0}}_\mu\chi^{\mathbf{g}}_\nu\big|\chi^{\mathbf{s}}_\sigma\chi^{\mathbf{s}+\mathbf{q}}_\rho\big), \tag{9}$$

where Mulliken notation for four-center integrals is used,

$$(\chi_\mu\chi_\nu|\chi_\sigma\chi_\rho) = \iint d\mathbf{r}_1 d\mathbf{r}_2 \frac{\chi_\mu(\mathbf{r}_1)\chi_\nu(\mathbf{r}_1)\chi_\sigma(\mathbf{r}_2)\chi_\rho(\mathbf{r}_2)}{|\mathbf{r}_1 - \mathbf{r}_2|}. \tag{10}$$

In Eq. (9), we have introduced the coefficients, in the AO basis, of the one-electron reduced density matrix (1RDM) computed by integration over the FBZ,

$$P^{\mathbf{q}}_{\sigma\rho} = \frac{1}{\Omega}\sum_i \int_{\mathrm{FBZ}} d\mathbf{k}\; e^{i\mathbf{k}\cdot\mathbf{q}} a^{\mathbf{k}}_{\sigma,i}\big[a^{\mathbf{k}}_{\rho,i}\big]^*\theta\big(\epsilon_F - \varepsilon^{\mathbf{k}}_i\big), \tag{11}$$

where Ω is the volume of the FBZ, θ is the Heaviside step function, representing the fractional occupation of the bands, and ϵ_F is the Fermi energy. For two-dimensional (2D) and 3D periodic systems, the Coulomb lattice series, whose electron-electron component is given in Eq. (9), is conditionally convergent. The series may be rendered absolutely convergent by Ewald summation techniques [38], employing a charge distribution of atom-centered point multipoles in the long range [39–42].

Within a generalized Kohn-Sham (GKS) framework [43,44], which allows for explicitly orbital-dependent functionals—as naturally occurring in hybrid forms, the matrix elements of the exchange-correlation contribution, in the AO basis, are obtained from the partial derivative of the xc energy functional $E_{\mathrm{xc}}[\{\psi_i\}]$ with respect to the elements of the density matrix introduced in Eq. (11),

$$\big[V^{\mathbf{g}}_{\mathrm{xc}}\big]_{\mu\nu} = \frac{\partial E_{\mathrm{xc}}}{\partial P^{\mathbf{g}}_{\mu\nu}}, \tag{12}$$

where E_{xc} is defined as

$$E_{\mathrm{xc}} = \int d\mathbf{r}\; \varepsilon_{\mathrm{c}}[n(\mathbf{r}), |\nabla n(\mathbf{r})|] + (1-\alpha)\int d\mathbf{r}\; \varepsilon_{\mathrm{x}}[n(\mathbf{r}), |\nabla n(\mathbf{r})|] + \alpha E_{\mathrm{exx}}[\{\psi_i\}], \tag{13}$$

and ε_{x} and ε_{c} are the exchange and correlation energy densities—which can be formulated according to different DFAs, $n \equiv n[\{\psi_i\}]$ is the particle-number density, and E_{exx} is the exact nonlocal Fock exchange energy, whose explicit expression is given in Eq. (15) below. A fraction α (in the range [0–1]) of the latter is included in hybrid DFAs. The rigorous theoretical foundation of the GKS approach is presented in Ref. [43] in DFT and in Ref. [45] in spin current density functional theory (SCDFT).

To summarize, we evaluate one- and two-electron integrals in direct space; see Eqs. (7)–(9) and (12) and (13). The overlap and Hamiltonian matrices are then transformed to reciprocal

space; see Eqs. (5) and (6), and Eq. (4) is solved. The corresponding eigenvalues and eigenvectors are then combined to calculate the coefficients of the 1RDM in the AO basis for the next SCF iteration; see Eq. (11). At each SCF iteration, the total electronic energy per unit cell is computed from

$$E_{\text{ele}} = \frac{1}{2}\sum_{\mu\nu}\sum_{\mathbf{g}} P^{\mathbf{g}}_{\mu\nu}\left(2M^{\mathbf{g}}_{\mu\nu} + C^{\mathbf{g}}_{\mu\nu}\right) + E_{\text{xc}}. \tag{14}$$

B. The exchange lattice series

In this section, we discuss the convergence of the exact exchange series and the criteria we adopt for an efficient direct space evaluation thereof, through truncation of the associated infinite lattice summations. It proves convenient to write down the expression for the exact exchange contribution to the electronic energy,

$$E_{\text{exx}} = -\frac{1}{2}\sum_{\mu\nu}\sum_{\mathbf{g}} P^{\mathbf{g}*}_{\mu\nu}\left[\sum_{\sigma\rho}\sum_{\mathbf{q}} P^{\mathbf{q}}_{\sigma\rho}\sum_{\mathbf{s}}\left(\chi^{\mathbf{0}}_{\mu}\chi^{\mathbf{s}}_{\sigma}\middle|\chi^{\mathbf{g}}_{\nu}\chi^{\mathbf{s}+\mathbf{q}}_{\rho}\right)\right]. \tag{15}$$

The exchange interaction is characterized by an overall slow decay with distance, which originates from the interplay between the decay of the two-electron integrals and the density matrix. Let us consider the leading exchange integrals in the AO basis. They have the form $(\chi^{\mathbf{0}}_{\mu}\chi^{\mathbf{0}}_{\mu}|\chi^{\mathbf{g}}_{\nu}\chi^{\mathbf{g}}_{\nu})$. The integral, applied in the limit of small Gaussian exponents (i.e., $\chi^{\mathbf{0}}_{\mu} = \chi^{\mathbf{g}}_{\nu} = 1$) and large separations (i.e., for large $|\mathbf{g}|$), reveal that individual contributions decay as $|\mathbf{g}|^{-1}$ at long range. At the same time, the number of interactions per unit distance grows as $|\mathbf{g}|^{D-1}$, where $D = 1, 2, 3$ is the periodic dimensionality of the system. Thus, overall, the leading AO exchange interaction for unit Gaussians grows as $|\mathbf{g}|^{D-2}$ at long range. Hence, it is clear that whether or not the exchange series may converge depends critically on the asymptotic behavior of the coefficients of the 1RDM $P^{\mathbf{g}}_{\mu\nu}$. For an insulator, these coefficients decay exponentially with the distance between two basis functions (the larger the band gap, the faster the decay) [46–50]. In conducting materials, the 1RDM has a more complex, oscillatory behavior, with a long-range polynomial decay where the coefficients of the polynomial are system dependent [51]. The precise analytical behavior has been explicitly worked out in the homogeneous limit [52].

The localized nature of the basis set allows for the effective evaluation of the exact exchange series of Eq. (15) in the following sense: (i) the AO coefficients of the 1RDM decay with increasing distance between two basis functions, as discussed above, and (ii) the overlap between two AOs decays exponentially with distance. These two properties significantly reduce the number of interactions that need to be considered. Efficient prescreening criteria can be devised in terms of the AO overlap to either truncate the series or partition it into distinct regions where the integrals can be computed exactly or approximately; see below.

1. Truncating

Inspection of Eq. (15) reveals the presence of three infinite lattice summations for the exact exchange energy. The summation over $\mathbf{s}$ can be effectively truncated from the exponential decay of $\chi^{\mathbf{0}}_{\mu}\chi^{\mathbf{s}}_{\sigma}$ and $\chi^{\mathbf{g}}_{\nu}\chi^{\mathbf{s}+\mathbf{q}}_{\rho}$. We employ an overlap criterion, which makes use of the *adjoined Gaussians* introduced below Eq. (3). The exchange integral is disregarded if either of the following overlaps are lower than a preset threshold $S_s = 10^{-T_s}$:

$$\left\langle G^{\mathbf{0}}_{\mu}\middle|G^{\mathbf{s}}_{\sigma}\right\rangle < S_s \quad \text{or} \quad \left\langle G^{\mathbf{g}}_{\nu}\middle|G^{\mathbf{s}+\mathbf{q}}_{\rho}\right\rangle > S_s, \tag{16}$$

where, for instance, $G^{\mathbf{g}}_{\nu}$ is the *adjoined Gaussian* of the shell that contains $\chi^{\mathbf{g}}_{\nu}$. We introduce a schematic representation of the truncation strategy for the exchange series in Fig. 1(a). For simplicity, we consider a 2D square lattice. The reference $\mathbf{g} = \mathbf{0}$ cell is highlighted in green. The four centers are marked by the corresponding AO indices. The radial extension of the associated adjoined Gaussians is schematically represented by blue circles. The lattice vectors are in magenta. In the example in Fig. 1(a), $G^{\mathbf{0}}_{\mu}$ and $G^{\mathbf{s}}_{\sigma}$ do overlap above the threshold S_s (red area), while $G^{\mathbf{g}}_{\nu}$ and $G^{\mathbf{s}+\mathbf{q}}_{\rho}$ do not.

The situation is more complicated for the first two summations in Eq. (15), over $\mathbf{g}$ and $\mathbf{q}$, whose effective truncation relies on the decay of the coefficients $P^{\mathbf{g}}_{\mu\nu}$ and $P^{\mathbf{q}}_{\sigma\rho}$, which

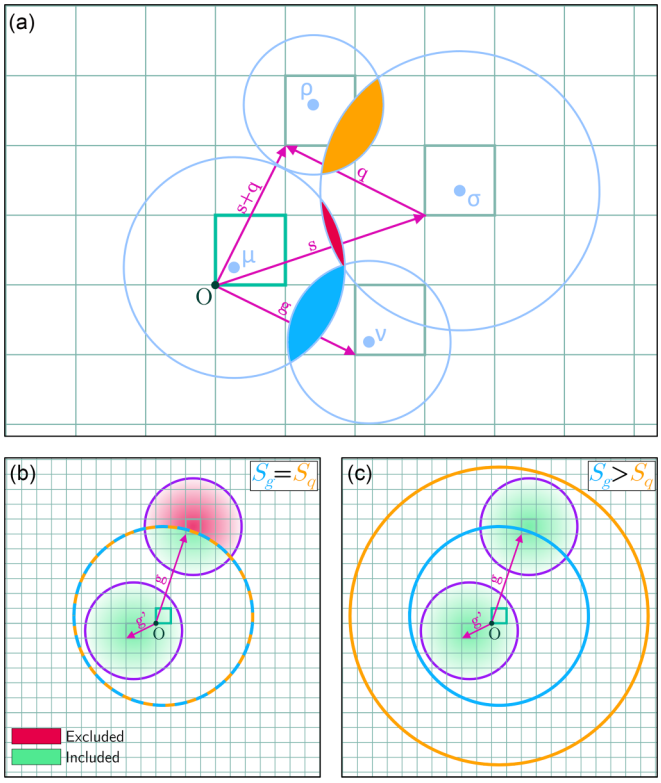

FIG. 1. (a) Schematic representation of the "direct space" truncation strategy for the exchange series with a localized basis set in a 2D square lattice. The reference $\mathbf{g} = \mathbf{0}$ cell is highlighted in green. The four centers of the exchange integrals are marked by the Greek letters of the corresponding AOs. The radial extension of the associated adjoined Gaussians is schematically represented by blue circles. The overlap between pairs of adjoined Gaussians is represented by color-filled areas. The lattice vectors of the different centers are given in magenta. (b) Schematic representation of the interplay between the S_g and S_q pseudo-overlap thresholds of Eq. (17) for $S_g = S_q$. (c) Same as in (b), but for $S_q < S_g$.

change during the SCF process. We adopt instead a so-called *pseudo-overlap* approach so that these two summations are truncated according to corresponding overlap integrals, via two preset thresholds $S_g = 10^{-T_g}$ and $S_q = 10^{-T_q}$:

$$\langle G_\mu^{\mathbf{0}} | G_\nu^{\mathbf{g}} \rangle < S_g \quad \text{and} \quad \langle G_\sigma^{\mathbf{0}} | G_\rho^{\mathbf{q}} \rangle < S_q. \tag{17}$$

This strategy exhibits two useful properties: (i) at variance with the density matrix elements, the overlap integrals remain fixed during the SCF process and thus tables of prescreened interactions can be compiled just once at the start of the calculation, and (ii) they take the same form of conditions (16) so that the same screening algorithm can be used for both. The above-mentioned truncation criteria are schematically represented in Fig. 1(a).

The pseudo-overlap approach of Eq. (17) requires some further analysis. At first glance, the truncation criteria for the **g** and **q** summations may look perfectly symmetrical and one might expect to set $S_g = S_q$, thus reducing the number of independent thresholds. However, the symmetry is broken by targeting accurate self-consistent solutions, which require an accurate self-consistent *potential* (we elaborate directly below). Let us analyze the exact-exchange potential in the AO basis, which is provided by the quantity within square brackets in Eq. (15). The leading contributions have the form $P_{\mu\nu}^{\mathbf{q}}(\chi_\mu^{\mathbf{0}}\chi_\mu^{\mathbf{0}}|\chi_\nu^{\mathbf{g}}\chi_\nu^{\mathbf{q}})$. Such contributions may be significant for small $|\mathbf{q} - \mathbf{g}|$ [i.e., within the purple circle in the schematic representation of Figs. 1(b) and 1(c)]. However, according to the criterion in Eq. (17), the **q** lattice vectors are selected as to be within a spherical region centered in the origin [see the yellow circle in Figs. 1(b) and 1(c)]. For large **g** vectors, the contributions from the red area in the figure would be disregarded by setting $S_g = S_q$ and this may be problematic if $P_{\mu\nu}^{\mathbf{q}}$ is large. To include contributions from the red area of the figure, we employ $S_q < S_g$.

2. The bipolar expansion

The electron-electron interaction can be simplified by the usual Neumann-Laplace expansion. In this approach, the Coulomb operator $1/|\mathbf{r}_1 - \mathbf{r}_2|$ is expanded around an origin $\mathbf{s}_1$ for electron 1 into a series of complex harmonics multiplied by radial factors. In the "bipolar" expansion approach, we go one step further and also expand around $\mathbf{s}_2$ for electron 2. The resulting double expansion provides an expression for the electron-electron interaction energy from simple multipole integrals [53–55]. More specifically, letting $\rho_1(\mathbf{r}_1 - \mathbf{s}_1) = \chi_\mu(\mathbf{r}_1)\chi_\nu(\mathbf{r}_1)$ and $\rho_2(\mathbf{r}_2 - \mathbf{s}_2) = \chi_\sigma(\mathbf{r}_2)\chi_\rho(\mathbf{r}_2)$ be two AO products, with centroids $\mathbf{s}_1$ and $\mathbf{s}_2$ (we recall that the centroid of the product of two Gaussian functions centered at $\mathbf{c}_\mu$ and $\mathbf{c}_\nu$, with exponents α_μ and α_ν, is $[\alpha_\mu\mathbf{c}_\mu + \alpha_\nu\mathbf{c}_\nu]/[\alpha_\mu + \alpha_\nu]$), $\mathbf{R} = \mathbf{s}_1 - \mathbf{s}_2$ the separation between the two distributions, and $R = |\mathbf{R}|$, $r_1 = |\mathbf{r}_1|$, $r_2 = |\mathbf{r}_2|$, in the limit of $R > r_1 + r_2$ (i.e., for well-separated, nonoverlapping distributions), the expansion takes the form [53]

$$\frac{1}{|\mathbf{r}_1 - \mathbf{r}_2|} = \sum_{l_1,l_2=0}^{\infty} \frac{1}{R^{2l_1+2l_2+1}} \sum_{m_1,m_2=-l_1,-l_2}^{l_1,l_2} B(l_1, m_1, l_2, m_2) Y_{l_1+l_2}^{-m_1-m_2}(\mathbf{R}) Y_{l_1}^{m_1}(\mathbf{r}_1 - \mathbf{s}_1) Y_{l_2}^{m_2}(\mathbf{r}_2 - \mathbf{s}_2), \tag{18}$$

with [40]

$$B(l_1, m_1, l_2, m_2) = (-1)^{\mathcal{M}} \frac{(l_1 + l_2 - |m_1 + m_2|)!}{(l_1 - |m_1|)!(l_2 - |m_2|)!}, \tag{19}$$

and where $\mathcal{M} = l_2 - m_1 - m_2 + 1/2(|m_1 + m_2| + |m_1| + |m_2|)$ and Y_l^m are unnormalized complex solid spherical harmonics. Insertion of Eq. (18) into Eq. (10) yields the following expression for two-electron integrals in the bipolar approximation,

$$(\chi_\mu\chi_\nu|\chi_\sigma\chi_\rho) = \sum_{l_1,l_2=0}^{\infty} \frac{1}{R^{2l_1+2l_2+1}} \sum_{m_1,m_2=-l_1,-l_2}^{l_1,l_2} B(l_1, m_1, l_2, m_2)\, Y_{l_1+l_2}^{-m_1-m_2}(\mathbf{R})\, \eta_{m_1}^{l_1}[\rho_1]\, \eta_{m_2}^{l_2}[\rho_2], \tag{20}$$

where $\eta_m^l[\rho] = \int d\mathbf{r}\rho(\mathbf{r})Y_l^m(\mathbf{r})$ [40]. A comparison of Eq. (20) with Eq. (10) reveals the simplification brought by the bipolar approximation in the evaluation of two-electron integrals: the double integral of Eq. (10) is substituted with the product of two single integrals in Eq. (20), which leads to a significant computational gain, to be assessed below. A criterion based on the overlap of the two distributions is used to determine whether the two-electron integral is computed exactly or via a truncated bipolar expansion, through a threshold $S_b = e^{-T_b}$,

$$\langle G_1 | G_2 \rangle < S_b, \tag{21}$$

where $G_1 = G_\mu \times G_\nu$ and $G_2 = G_\sigma \times G_\rho$ are the products of the two adjoined Gaussians for the first and second distribution, respectively.

3. The range separation

A popular approach to circumvent the slow decay of the exchange interaction in large molecules and extended solids is represented by a splitting of the $1/|\mathbf{r}_1 - \mathbf{r}_2|$ Coulomb operator of Eq. (10) into a short-range (SR) and a long-range (LR) component,

$$\frac{1}{|\mathbf{r}_1 - \mathbf{r}_2|} = \underbrace{\frac{\mathrm{erfc}(\omega|\mathbf{r}_1 - \mathbf{r}_2|)}{|\mathbf{r}_1 - \mathbf{r}_2|}}_{\mathrm{SR}} + \underbrace{\frac{\mathrm{erf}(\omega|\mathbf{r}_1 - \mathbf{r}_2|)}{|\mathbf{r}_1 - \mathbf{r}_2|}}_{\mathrm{LR}}, \tag{22}$$

and by neglecting the LR component in the exact-exchange integrals, compensated by a LR contribution from an exchange DFA [19,20]. In Eq. (22), $\mathrm{erfc}(a) = 1 - \mathrm{erf}(a)$ is the complementary error function and ω is a range-separation parameter. Hybrid DFAs built from this prescription have become very

popular because of significant computational gains in plane-wave electronic structure simulations of materials [25].

III. COMPUTATIONAL DETAILS

All calculations are performed with a developmental version of the CRYSTAL23 electronic structure package [56], where the LCAO approach described in Sec. II is implemented. The basis sets of GTFs used in this study are reported in the electronic Supplemental Material (SM) [57], along with the description of the Monkhorst-Pack mesh of **k** points used in the sampling of reciprocal space for the various investigated systems. We use the Perdew-Burke-Ernzerhof (PBE) [58] exchange-correlation functional from the generalized-gradient approximation (GGA), and its globally hybridized version, popularized by PBE0 [5], through a fraction α of nonlocal Fock exchange. The value of $\alpha = 0.15$ is used for some systems for reasons to be elaborated in Sec. IV. We refer to such global hybrid DFA as PBE(15) in what follows [59]. Additionally, the Heyd-Scuseria-Ernzerhof range-separated hybrid functional is used, in its HSE06 parametrization, with $\omega = 0.11$ Bohr^{-1} in Eq. (22) [19]. For reasons discussed at the end of Sec. II B 1, the default setting $T_q = 2T_g$ is used for all calculations reported in the main text of the manuscript. Let us note that neglected long-range contributions to the exchange series in HSE06 should make it possible to safely work with a lower value for the T_q threshold, reducing its cost with little loss in accuracy. When the bipolar approximation is used, we include terms with $l_1, l_2 = 0, 1, 2$ in Eq. (20).

The energy convergence criterion for the self-consistent field (SCF) procedure is set to the tight value of 10^{-9} hartree. Unless stated otherwise, all structures are fully relaxed (atomic positions and lattice parameters) through a quasi-Newton geometry optimization with Broyden-Fletcher-Goldfarb-Shanno Hessian updating [60]. Pressure-constrained geometry optimizations are performed through the analytical evaluation of the stress tensor [61,62]. A replicated-data parallel version of the program, pcrystal, using message-passing-interface (MPI) directives, is used [63–66].

All calculations are performed on the Data Centric General Purpose partition of the Leonardo HPC, featuring nodes equipped with two Intel Saphire Rapids processors (2×56 cores, 2.0 GHz) and 512 GB of DDR5 Memory. The parallelization of the code is achieved with the use of MPI (from Intel oneapi 2021.10.0 package).

Relativistic operators are included through RECPs. Spin-orbit coupling (SOC) integrals are computed analytically for both the energy [67] and forces [68]. SOC is treated self-consistently within a two-component formal framework for local-density, generalized-gradient, meta-generalized-gradient, and global hybrid DFAs [30,45,69–73]. The SOC implementation has been extended to range-separated hybrid DFAs for this work.

IV. RESULTS AND DISCUSSION

We discuss the efficiency of the methodology outlined in Sec. II with respect to three systems that have been selected so as to be representative of different regimes where the effect of Fock exchange should be assessed. The first system is bulk (3D) hematite, α-Fe_2O_3, in its insulating, antiferromagnetic configuration with about four unpaired electrons in the d-type orbitals on each Fe center. We perform all-electron calculations. The second system is the semiconducting single-layer (2D) WSe_2, which exhibits a giant type-I Rashba spin splitting at the top of the valence band induced by the interplay of space inversion symmetry breaking, and time-reversal symmetry preservation, together with large SOC [74]. We perform calculations with RECPs for an effective inclusion of scalar+SOC relativistic effects. The third system is bulk (3D) EuO in its metallic phase at a pressure of 20 GPa. Indeed, EuO in its B1 structure undergoes an isostructural, insulator-to-metal phase transition at around 10–15 GPa [75]. The system is ferromagnetic with seven unpaired electrons hosted by f-type orbitals of each Eu atom.

We investigate the effect of Fock exchange on several electronic properties of the selected systems, and we analyze the convergence of the exchange series with respect to the truncation criteria introduced in Sec. II B 1. The numerical stability and computational efficiency of the bipolar approximation introduced in Sec. II B 2 is assessed. Speed-up in the evaluation of two-electron exchange integrals from parallel computing is reported, and scaling with respect to system size is analyzed by building supercells (up to 640 atoms/cell for hematite, 75 atoms/cell for WSe_2, and 128 atoms/cell for EuO).

A. Hematite Fe_2O_3

We study the hexagonal phase (space group $R\bar{3}c$) of hematite, α-Fe_2O_3, in its antiferromagnetic collinear spin ground-state configuration. All calculations are performed on the primitive cell containing 10 atoms (i.e., two formula units), unless otherwise specified. Reciprocal space is sampled in a $12 \times 12 \times 12$ Monkhorst-Pack mesh of **k** points. Results are shown in Fig. 2 from PBE, PBE(15), and HSE06 calculations. For the global hybrid DFA, the value of $\alpha = 0.15$ for the fraction of exact exchange in Eq. (13) is determined by following the prescription according to which $\alpha = 1/\epsilon_\infty$ should be the inverse of the static electronic dielectric constant of the material [7,8,14,15]. The experimental value of ϵ_∞ for hematite is approximately 7 [76].

The electronic band structure of α-Fe_2O_3 is shown in Fig. 2(b) as obtained from PBE (blue), PBE(15) (green), and HSE06 (purple) calculations. The band gap predicted by PBE, 0.55 eV, largely underestimates the experimental band gap of 2.6 eV, which is consistent with previous plane-wave results [77–79]. This is mainly due to the self-interaction error and the related overdelocalization of valence electrons [77]. HSE06 overestimates the band gap, 3.35 eV (again consistently with previous plane-wave calculations [79]), while PBE(15) provides an excellent description of the electronic band structure, with a predicted band gap of 2.65 eV, as already noted [78]. Figure 2(a) reports a graphical representation of the spin density distribution, along with the computed magnetic moments on the Fe atoms: 3.86, 4.24, and 4.34 μ_B from PBE, PBE(15), and HSE06, respectively. The lower value from PBE is consistent with the above-mentioned overdelocalization and therefore lower ionicity of the solution.

In Figs. 2(c) and 2(d), we analyze the convergence of the exchange series in direct space with respect to the truncation

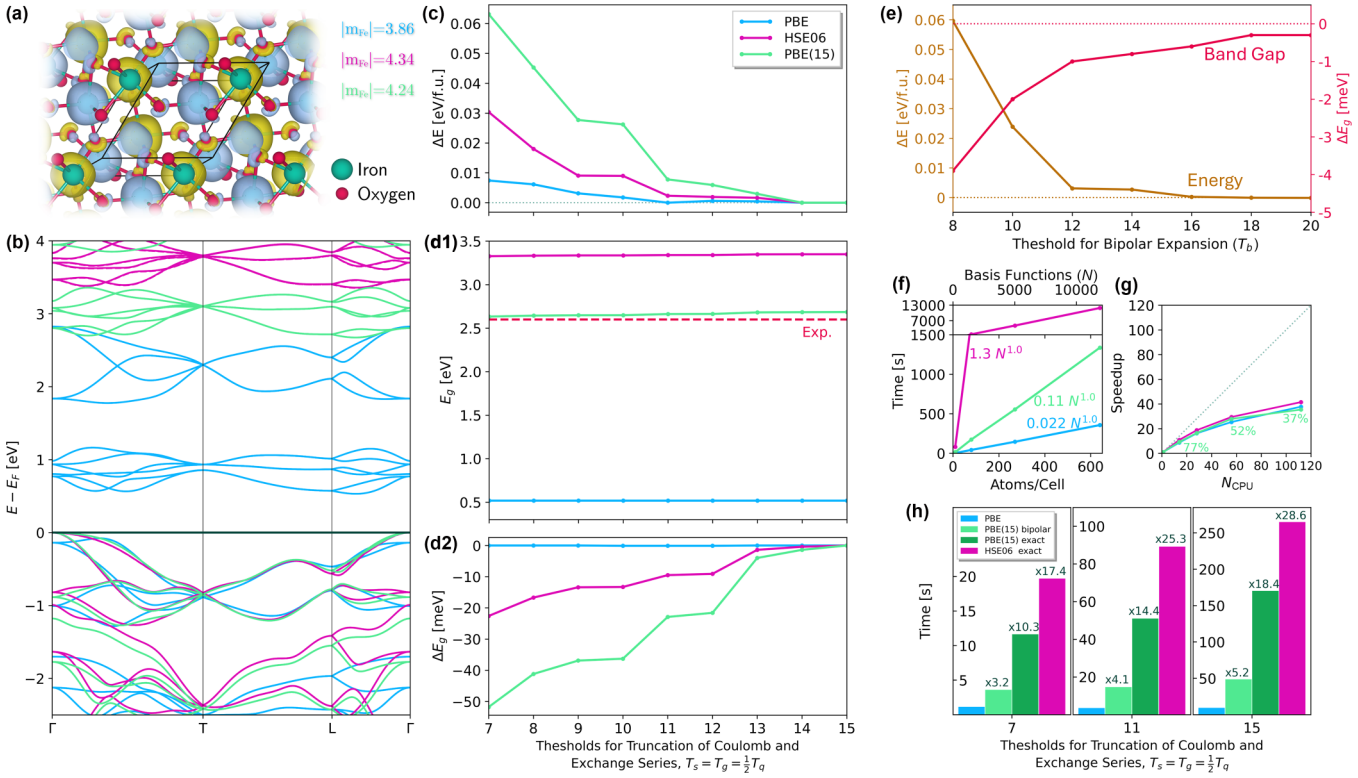

FIG. 2. Effect of exact Fock exchange on Hematite, α-Fe_2O_3. (a) Graphical representation of the 3D spatial distribution of the spin density in the antiferromagnetic collinear ground-state configuration (yellow and blue surfaces correspond to regions of positive and negative spin density, respectively). The absolute values of computed magnetic moments on the Fe atoms, $|m_{\mathrm{Fe}}|$, are also reported (in μ_{B}) from PBE (blue), PBE(15) (green), and HSE06 (purple). (b) Electronic band structure computed with PBE (blue), PBE(15) (green), and HSE06 (purple). (c) Convergence of the total electronic energy with respect to truncation criteria of the exchange series; the energy difference ΔE with respect to an almost converged $T_s = T_g = \frac{1}{2}T_q = 15$ setting is reported (in eV per formula unit). (d) Convergence of the computed band gap E_g with respect to truncation criteria of the exchange series; absolute values in (d1) and differences with respect to an almost converged $T_s = T_g = \frac{1}{2}T_q = 15$ setting in (d2). In (c) and (d), the bipolar expansion is used for PBE and PBE(15) calculations. (e) Convergence of the PBE(15) energy and band gap as a function of the threshold T_b according to which two-electron exchange integrals are computed exactly or via the bipolar expansion. The other thresholds are set to $T_s = T_g = \frac{1}{2}T_q = 11$. (f) Time needed to compute two-electron integrals as a function of system size (supercells containing 10, 80, 270, 640 atoms are explored), with a fixed number of CPU cores, $N_{\mathrm{CPU}} = 112$. (g) Speedup in the calculation of two-electron integrals as a function of the number of CPU cores used. (h) Time needed to compute two-electron integrals for PBE, PBE(15), and HSE06 calculations. For the full range hybrid calculation, PBE(15), two values are reported (light- and dark-green bars), which correspond to using the bipolar approximation or not.

criteria introduced in Sec. II B 1. On the x axis, we have the values of the T_s and T_g thresholds, while T_q here is always set to twice the value of T_g, so that $T_s = T_g = \frac{1}{2}T_q$. See Eqs. (16) and (17) for a formal definition of the thresholds. In particular, in Fig. 2(c), we analyze the convergence of the total electronic energy of Eq. (14). The energy difference ΔE with respect to an almost converged setting of $T_s = 15$ is reported (in eV per formula unit). The following is observed: (i) the convergence of the Coulomb series in the PBE calculation (blue line) is very fast. Although not explicitly discussed, overlap-based truncation criteria analogous to those in Eq. (16) are implemented for the Coulomb direct space series; (ii) the convergence of the unscreened exact-exchange series (green line) is slower (as expected) and is still characterized by a monotonic trend with respect to the overlap and pseudo-overlap criteria discussed in Sec. II B 1; and (iii) convergence of the exchange series becomes faster with HSE06 (purple line) because of range separation and the associated neglect of the long-range term in Eq. (22), again as expected. Given the arbitrary nature of the pseudo-overlap truncation criteria of Eq. (17), the absence of oscillations in the observed convergence for the full range hybrid calculations is noteworthy. Figure 2(d) reports the analogous convergence of the computed band gap E_g. On the scale of the computed property, the three lines appear to be almost perfectly horizontal at 0.55 eV for PBE, 2.65 eV for PBE(15), and 3.35 eV for HSE06. This implies that even relatively low values of the truncation thresholds provide converged band gaps within 0.1 eV. The bottom panel shows the difference of computed band gaps relative to an almost converged setting of $T_s = 15$, to better appreciate the convergence of E_g as a function of the exchange series truncation. The slow and monotonic convergence of PBE(15) already discussed on the energy is also observed on the band gap. Note that here the band gap is slowly changing on the order of 10^{-2} eV. Thus, while "fully converged" electronic structure predictions may require the truncation

thresholds to be pushed to values of $T_s = 13$, default settings of $T_s = 7$ already allow one to catch most of the physics of the exact-exchange interactions. We will get back to these aspects soon when discussing the associated computational costs.

In Fig. 2(e), we analyze the effect of the bipolar expansion described in Sec. II B 2. In particular, we report the convergence of the energy and band gap of α-Fe_2O_3 as a function of the overlap-based threshold T_b according to which two-electron exchange integrals are computed exactly as in Eq. (10) or via the bipolar expansion as in Eq. (20). At $T_b = \infty$, all integrals are computed exactly. In the figure, we report differences in energy and band gaps relative to this exact limit. The following is observed: (i) both the energy and the band gap vary monotonically with T_b, and rapidly converge; (ii) at $T_b = 12$, the energy is basically converged within 3 meV per formula unit, and the band gap within 1 meV. We shall document the computational gain associated to the bipolar approximation below.

Figure 2(f) reports the time needed to compute two-electron integrals for PBE, PBE(15), and HSE06 calculations as a function of system size (supercells containing 10, 80, 270, and 640 atoms are explored), with a fixed number of CPU cores, $N_{\mathrm{CPU}} = 112$, corresponding to a full node. Data are fitted to a function of the type aN^b, where N represents the number of basis functions used. *Linear scaling* (i.e., $b = 1.0$) is observed in all calculations, as expected from the translational invariance of the direct space lattice. The prefactors a span values from 0.02 of PBE to 0.11 of PBE(15) to 1.5 of HSE06, suggestive of different associated costs, to be further inspected and discussed below. Figure 2(g) reports the speedup in the calculation of two-electron integrals of the primitive cell (10 atoms) as a function of the number of CPU cores used. The time is systematically reduced by use of more CPU cores, although not ideally because of the small size of the system. Higher speedups are expected for larger systems [66].

Finally, let us analyze timings so as to assess the computational efficiency of our strategy for direct space treatment of the exchange series. Figure 2(h) reports the time needed to compute two-electron integrals for PBE, PBE(15), and HSE06 calculations. For the full range hybrid calculation, PBE(15), two values are reported, which correspond to using the bipolar approximation or not using it. The three panels in Fig. 2(h) correspond to different settings for the truncation thresholds T_s, T_g, and T_q. Calculations are performed on a full node (i.e., 112 CPU cores) of the architecture described in Sec. III. Detailed timings are also tabulated in Table S1 of SM [57]. As a reference, the calculation takes 1.1 seconds for PBE (blue bar in the figure) with default settings (i.e., $T_s = 7$). The full range hybrid, PBE(15), calculation only takes 3.6 seconds when the truncation strategy of the exchange series discussed in Sec. II B 1 and the bipolar approximation discussed in Sec. II B 2 are used (light-green bar). That is, the cost of a full hybrid calculation is just 3.2× that of a plain GGA within our direct space approach. If the bipolar approximation is switched off, the cost increases to 11.6 seconds (dark-green bar). That is, the bipolar approximation contributes to the reduction of the cost of the evaluation of two-electron exchange integrals by a factor of 1/3. The time needed to compute two-electron integrals with HSE06 is 19.7 seconds (purple bar). Going back to Fig. 2(h), when the truncation thresholds T_s, T_g, and T_q for the exchange series are increased, the cost of the evaluation of two-electron integrals increases accordingly. This is documented in the other panels of Fig. 2(h) for $T_s = 11$ and $T_s = 15$. However, key aspects do not change: (i) the effect of the bipolar approximation is always to reduce the time by a factor between 1/3 and 1/4; (ii) the cost of a full range hybrid calculation relative to a plain GGA one just passes from 3.2× to 4.1× and 5.2×. Needless to say, these factors are particularly impressive when compared to those experienced from plane-wave implementations, where factors of 100×–1000× are common and such to make global hybrids "almost intractable" [25]. We note that larger factors are also not uncommon from implementations based on local basis sets. For instance, a factor of about 100× has recently been reported on the same test system (hematite, α-Fe_2O_3) using numeric atom-centered orbitals and direct space resolution-of-identity for the exchange series; see Table V in Ref. [34].

B. Single-layer WSe_2

We study the semiconducting single-layer (2D) transition-metal dichalcogenide WSe_2, whose atomic structure is represented in Fig. 3(a). Let us note in passing that the use of a local, atom-centered, basis set allows us to model such low-dimensional systems without the need to replicate their structure along nonperiodic directions. Calculations are performed on the primitive 2D cell containing three atoms, unless otherwise specified. Space inversion symmetry breaking and time-reversal symmetry preservation, together with a large spin-orbit coupling (SOC), induce a giant Rashba type-I spin splitting at the top of the valence band in single-layer WSe_2; a value of $\Delta_v = 513 \pm 10$ meV has been measured at the K point of the first Brillouin zone via angle-resolved photoemission spectroscopy [80]. We report the computed electronic band structure in Fig. 3(b), where the region of the Rashba splitting Δ_v is highlighted in yellow. In the absence of SOC, the two topmost valence bands would be fully degenerate (i.e., Δ_v would be 0), while with SOC, the degeneracy is broken along the Γ-K-M path, with the maximum splitting occurring at point K. The figure shows the electronic structure provided by different density functional approximations: PBE, PBE(15), and HSE06. The optimal value of $\alpha = 0.15$ for the fraction of Fock exchange has been selected based on a previous investigation [74]. Based on experimental evidence, single-layer WSe_2 likely exhibits two nearly degenerate band gaps: a direct band gap at K and an indirect one from K to Q (i.e., a point lying close to the midpoint along the Γ-K path). Scanning tunneling spectroscopy measurements provide a value of 2.12 ± 0.06 eV [81]. Inspection of Fig. 3(b) shows that our calculations confirm the near degeneracy of such transitions. With PBE (blue lines), the band gap is significantly underestimated at about 1.4 eV. As expected, hybrid DFAs do a better job at describing the band gap with HSE06 at about 1.87 eV and PBE(15) at 2.02 eV.

Apart from the expected different description of the band gap, the Rashba splitting is also significantly affected by the DFA. To this end, it is worth noting that the giant Rashba type-I spin splitting of 513 ± 10 meV is systematically underestimated by about 10–15% with standard (semi)local DFAs

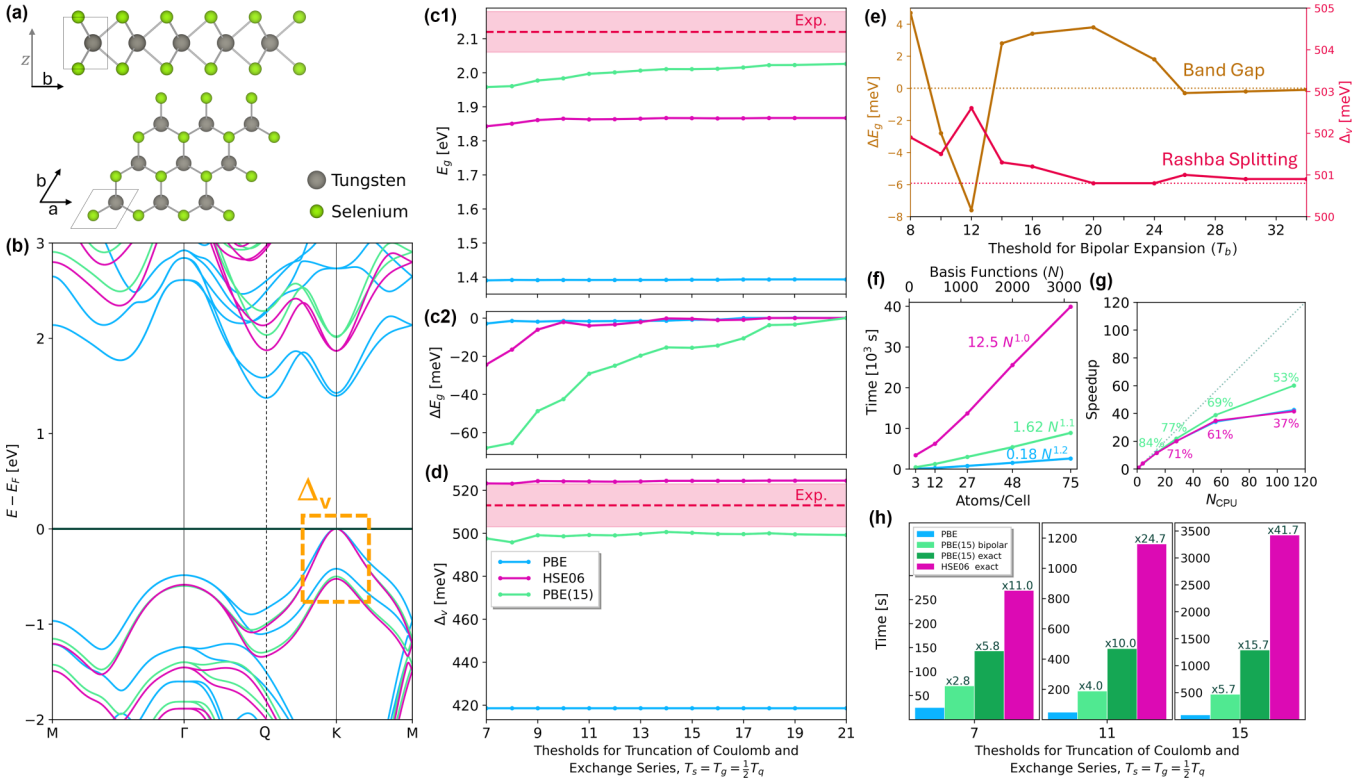

FIG. 3. Effect of exact Fock exchange on single layer WSe_2. (a) Graphical representation of the 2D structure. (b) Electronic band structure computed with PBE (blue), PBE(15) (green), and HSE06 (purple); the region of the Rashba type-I splitting is highlighted in yellow. (c) Convergence of the computed band gap with respect to truncation criteria of the exchange series; absolute values in (c1) and differences with respect to an almost converged $T_s = T_g = \frac{1}{2}T_q = 21$ setting in (c2). (d) Same as in (c1), but for the computed Rashba splitting Δ_v. In (c) and (d), the bipolar expansion is used for PBE and PBE(15) calculations. (e) Convergence of the PBE(15) band gap and Rashba splitting as a function of the threshold T_b according to which two-electron exchange integrals are computed exactly or via the bipolar expansion. The other thresholds are set to $T_s = T_g = \frac{1}{2}T_q = 11$. (f) Time needed to compute two-electron integrals as a function of system size (supercells containing 3, 12, 27, 48, and 75 atoms are explored), with a fixed number of CPU cores, $N_{CPU} = 112$. (g) Speedup in the calculation of two-electron integrals as a function of the number of CPU cores used. (h) Time needed to run one SCF cycle for PBE, PBE(15), and HSE06 calculations. For the full range hybrid calculation, PBE(15), two values are reported (light- and dark-green bars), which correspond to either using the bipolar approximation or not using it.

within the DFT framework [80,82–85]. Our calculations confirm this trend with the PBE predicted value of 419 meV underestimating the experiment by 18%. On the contrary, hybrid DFAs provide values of 500 and 521 meV from PBE(15) and HSE06, respectively.

In Figs. 3(c) and 3(d), we analyze the convergence of the exchange series in direct space with respect to the truncation criteria introduced in Sec. II B 1. In particular, in Fig. 3(c), we analyze the convergence of the computed band gap (the experimental value is reported as a red horizontal dashed line). As expected, the convergence of the Coulomb series in the PBE calculation (blue line) is very fast. The convergence of the unscreened exact-exchange series (green line) is much slower, but remarkably monotonic. Convergence of the exchange series is consistently accelerated with HSE06 (purple line) because of the neglected long-range term in Eq. (22). Figure 3(d) reports the analogous convergence of the computed Rashba splitting Δ_v (again, the experimental value is marked by a red dashed horizontal line). On the scale of the computed property, the three lines appear to be almost perfectly horizontal, apart from some noise in the PBE(15) data at very low values of the truncation thresholds.

In Fig. 3(e), we analyze the convergence of the band gap and Rashba splitting as a function of the overlap-based threshold T_b according to which two-electron exchange integrals are computed exactly as in Eq. (10) or via the bipolar expansion as in Eq. (20). We recall that at $T_b = \infty$, all integrals are computed exactly. For the band gap, we report differences relative to this exact limit. The following is observed: (i) both the band gap and the Rashba splitting show a "spike" at $T_b = 12$ and converge at $T_b \geqslant 26$; (ii) even at $T_b = 14$ (the default value), the band gap is basically converged within 2 to 3 meV, and the Rashba splitting within 0.5 meV. We shall document the computational gain associated to the bipolar approximation below.

Figure 3(f) reports the time needed to compute two-electron integrals for PBE, PBE(15), and HSE06 calculations as a function of system size (supercells containing 3, 12, 27, 48, and 75 atoms are explored), with a fixed number of CPU cores, $N_{CPU} = 112$, corresponding to a full node. As expected, the scaling is close to linear in all cases, with powers of 1.0, 1.1, and 1.2 for HSE06, PBE(15), and PBE, respectively. The prefactors span values from 0.18 of PBE to 1.62 of PBE(15) to 12.5 of HSE06, indicative of different associated costs, to

be further discussed below. Figure 3(g) reports the speedup in the calculation of two-electron integrals of the primitive cell as a function of the number of CPU cores used. The time is systematically reduced by use of more CPU cores, although not ideally because of the small size of the system [66].

We assess the computational efficiency of our strategy for direct space treatment of the exchange series in Fig. 3(h), where we report the time needed to perform one SCF iteration for PBE, PBE(15), and HSE06 calculations. For the full range hybrid calculation, PBE(15), two values are reported, which correspond to either using or not using the bipolar approximation. The three panels in Fig. 3(h) correspond to different settings for the truncation thresholds T_s, T_g, and T_q. Calculations are performed on a full node (i.e., 112 CPU cores) of the computing cluster described in Sec. III. Detailed timings are also tabulated in Table S2 of SM [57]. As a reference, the calculation takes 24.5 seconds for PBE (blue bar in the figure) with default settings (i.e., $T_s = 7$). The full range hybrid, PBE(15), calculation only takes 69.7 seconds when the truncation strategy of the exchange series discussed in Sec. II B 1 and the bipolar approximation discussed in Sec. II B 2 are used (light-green bar). That is, the cost of a full hybrid calculation is just 2.8× that of a plain GGA within our direct space approach. If the bipolar approximation is switched off, the cost increases to 142.5 seconds (dark-green bar). That is, the bipolar approximation contributes to the overall reduction of the cost of an SCF iteration by a factor of 1/2. The time for an HSE06 calculation is 268.5 seconds (purple bar). As noted above, we have not yet implemented the bipolar approximation for range-separated hybrids. When the truncation thresholds T_s, T_g, and T_q for the exchange series are increased, the cost of the calculation increases, as does the gain from the use of the bipolar approximation (passing from a factor of 2 to a factor of 3). The cost of a full range hybrid calculation relative to a plain GGA one just passes from 2.8× to 4.0× and 5.7×.

C. High-pressure metallic ferromagnetic EuO

We study bulk ferromagnetic EuO in its high-pressure $Fm\bar{3}m$ metallic phase, at 20 GPa [86,87]. Calculations are performed on the primitive cell containing two atoms, unless otherwise specified. The simultaneous presence of itinerant states and highly localized electrons (seven unpaired electrons in half-filled $4f$ orbital shells on each Eu atom) makes it a mixed-valence system, which benefits from the inclusion of a fraction of exact Fock exchange [75].

EuO, both in its native and multiferroic phases, exhibits a variety of fascinating electronic properties [88]. In this study, we have selected it because it represents a formidable stress test to our approach. Indeed, having a high density (at a pressure of 20 GPa) and a metallic character, this system is expected to exhibit a very slow decay of the exact-exchange series in direct space of Eq. (15). We shall illustrate how our truncation/approximation strategy works on this system below, with results shown in Fig. 4.

The effect of the truncation criteria introduced in Sec. II B 1 is analyzed in Figs. 4(b)–4(d) on the electronic band structure, energy, and magnetic spin moment, respectively. The electronic band structure is inspected in the vicinity of the Fermi energy as computed with the hybrid PBE0 xc functional and for different values of the truncation thresholds T_s, T_g, and T_q (corresponding to different shades of green). The changes in the band structure are small and regular. As the thresholds are tightened, changes become smaller until the band structure nicely converges. The spin magnetic moment is very little affected by the truncation thresholds [see almost horizontal lines in Fig. 4(d)] for different types of xc functionals (PBE, PBE0, and HSE06). The total energy of the system is the most sensitive property in this context, and yet it evolves with a remarkable regular monotonic trend with respect to the truncation thresholds, with both PBE and HSE06 reaching convergence at $T_s = T_g = \frac{1}{2}T_q = 27$, a value at which the PBE0 series also exhibits a change in the slope and partially flattens.

In Fig. 4(e), we analyze the convergence of the total energy and spin magnetic moment as a function of the overlap-based threshold T_b according to which two-electron exchange integrals are computed exactly as in Eq. (10) or via the bipolar expansion as in Eq. (20). At $T_b = \infty$, all integrals are computed exactly. We plot differences relative to this exact limit. The following is observed: (i) both quantities seem to converge at $T_b = 30$; (ii) even at $T_b = 14$ (the default value), the spin magnetic moment is basically converged within $4\,\mathrm{m}\mu_\mathrm{B}$ and the energy within 1 meV. We shall document the computational gain associated to the bipolar approximation for this system below.

Figure 4(f) reports the time needed to compute two-electron integrals for PBE and PBE0 calculations as a function of system size (supercells containing 2, 16, 54, and 128 atoms are explored), with a fixed number of CPU cores, $N_\mathrm{CPU} = 112$, corresponding to a full node. Linear scaling is again confirmed, with powers of 1.0 and 1.1 for PBE0 and PBE, respectively. The prefactors are 0.055 for PBE and 0.85 for PBE0, indicative of different associated costs, to be discussed below. Figure 4(g) reports the speedup in the calculation of two-electron integrals of the primitive cell as a function of the number of CPU cores used. The time is systematically reduced by the use of more CPU cores, although not ideally because of the small size of the system (just two atoms per cell) [66].

The computational efficiency of our strategy for direct space treatment of the exchange series is assessed in Fig. 4(h) for the EuO case, where we report the time needed to perform one SCF iteration for PBE, PBE0, and HSE06 calculations. For the full range hybrid calculation, PBE0, two values are reported, which correspond to using or not using the bipolar approximation. The four panels in Fig. 4(h) correspond to different settings for the truncation thresholds T_s, T_g, and T_q. Calculations are performed on a full node (i.e., 112 CPU cores) of the computing cluster described in Sec. III. Detailed timings are also tabulated in Table S3 of SM [57]. As a reference, the calculation takes 4.1 seconds for PBE (blue bar in the figure) with default settings (i.e., $T_s = 7$). The full range hybrid, PBE0, calculation only takes 24.3 seconds when the truncation strategy of the exchange series discussed in Sec. II B 1 and the bipolar approximation discussed in Sec. II B 2 are used (light-green bar). That is, the cost of the full hybrid calculation is just 5.9× that of a plain GGA within our direct space approach. As expected, this factor of 5.9 is larger than those observed for the previous two tests cases

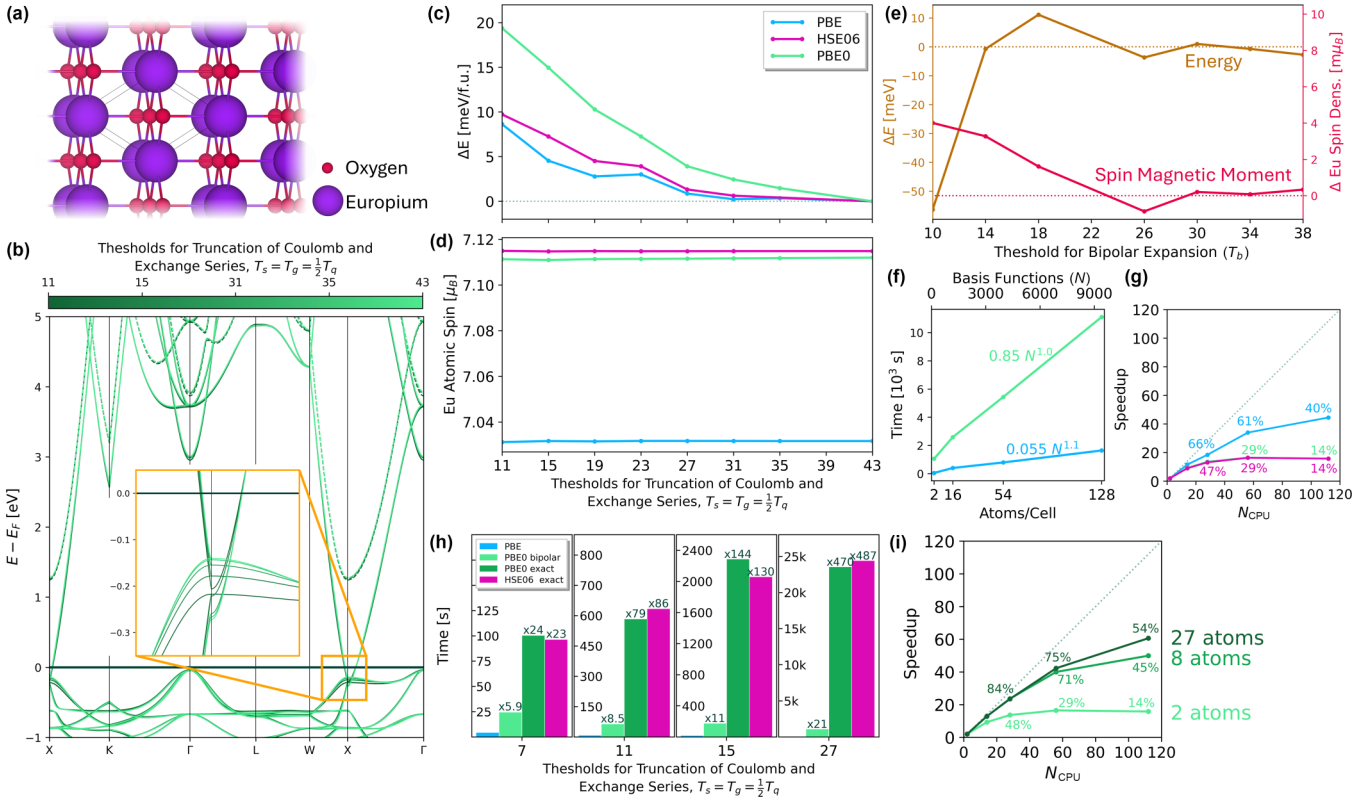

FIG. 4. The effect of exact Fock exchange on bulk ferromagnetic EuO at 20 GPa of pressure. (a) Graphical representation of the atomic structure. (b) Electronic band structure from PBE0 calculations for different truncation thresholds of the exchange series. (c) Convergence of the total electronic energy with respect to truncation criteria of the exchange series; the energy difference ΔE with respect to an almost converged $T_s = T_g = \frac{1}{2}T_q = 43$ setting is reported (in meV per formula unit). (d) Convergence of Eu spin magnetic moment. In (c) and (d), the bipolar expansion is used for PBE and PBE(15) calculations. (e) Convergence of the total energy and spin magnetic moment as a function of the threshold T_b according to which two-electron exchange integrals are computed exactly or via the bipolar expansion, from PBE0 calculations. The other thresholds are set to $T_s = T_g = \frac{1}{2}T_q = 27$. (f) Time needed to compute two-electron integrals as a function of system size (supercells containing 2, 16, 54, and 128 atoms are explored), with a fixed number of CPU cores, $N_{CPU} = 112$. (g) Speedup in the calculation of two-electron integrals as a function of the number of CPU cores used. (h) Time needed to run one SCF cycle for PBE, PBE0, and HSE06 calculations. For the full range hybrid calculation, PBE0, two values are reported (light- and dark-green bars), which correspond to using the bipolar approximation or not using it. (i) Same as (g), for PBE0 on different supercells.

(3.2 for Hematite and 2.8 for single-layer WSe_2). Indeed, let us recall that this system (dense, metallic) has been selected to be as challenging as possible for our approach. If the bipolar approximation is switched off, the cost increases to 100.3 seconds (dark-green bar). That is, the bipolar approximation contributes to the overall reduction of the cost of an SCF iteration by a factor of 4.1. The time for an HSE06 calculation is 96.1 seconds (purple bar). As already noted above, we have not yet implemented the bipolar approximation for range-separated hybrids. When the truncation thresholds T_s, T_g, and T_q for the exchange series are increased, the cost of the calculation increases, as does the gain from the use of the bipolar approximation (passing from a factor of 4.1 to a factor of 9.6, 13.5, and 24.6 for $T_s = T_g = \frac{1}{2}T_q$ 11, 15, and 27, respectively).

Finally, let us note that the current implementation of HSE06 lacks the bipolar approximation and that calculations are performed within the $T_q = 2T_g$ setting, which may be unfavorable for HSE06. Lower values of T_q should result in a reduced cost with little accuracy loss. To tentatively quantify the expected reduction in cost, we have performed preliminary calculations to explore the effect of setting $T_q = T_g$ in HSE06 calculations on EuO. Results are presented in Sec. 4.5 of SM [57], where a reduction in cost by a factor of two is documented.

V. CONCLUSIONS AND PERSPECTIVES

A direct space approach to the evaluation of exact nonlocal Fock exchange in periodic systems has been reviewed, based on localized, atom-centered, Gaussian-type basis functions, where core electrons are treated either explicitly (all-electron approach) or through relativistic effective core potentials. An efficient prescreening strategy in terms of the localized basis is discussed to either truncate the series via overlap-based criteria or partition it into distinct regions where the integrals can be computed exactly or approximately via a bipolar expansion of the Coulomb operator.

Application to hybrid density functional approximations—both in their global and range-separated versions—is discussed and their efficiency assessed with respect to the generalized-gradient approximation. Three test systems are

considered, which were selected to span different electronic regimes: (i) bulk hematite, α-Fe_2O_3, in its insulating, antiferromagnetic configuration; (ii) semiconducting single-layer WSe_2 (with inclusion of spin-orbit coupling); and (iii) bulk EuO in its metallic ferromagnetic phase at a pressure of 20 GPa. The direct space screening strategy behaves very regularly in all regimes, with rather monotonic trends, including the stress test of highly dense metallic EuO.

A relative cost of just 3–6 times—across different electronic regimes—of the global hybrid approximation relative to the generalized-gradient approximation is documented. Thus, this approach allows for higher accuracy—by climbing to the fourth rung of Jacob's ladder of density functional approximations, as put forward by Perdew—at a cost that is comparable to that of approximations from the first two rungs.

A large part of this manuscript is devoted to the analysis of the convergence of the exact-exchange series in a local basis set in terms of overlap-based truncation criteria to show how "fully converged" or "close to fully converged" results can be obtained. At the same time, let us stress that from a practical standpoint, for the simulation of many properties of materials—such as band gaps, spin magnetic moments, Rashba splittings, just to restrict to those explicitly investigated in this manuscript—the type (hybrid versus nonhybrid) of density functional approximation does affect the results to a much larger extent than the specifics of the truncation of the exact-exchange series do. That is, most of the physics of the exact-exchange interaction is already captured by "loose" convergence thresholds, with an associated low(er) computational cost.

The implementation of range-separated hybrid functionals has been generalized to include spin-orbit coupling within a two-component self-consistent framework, without the bipolar approximation. The efficiency of short-range hybrid functionals, as those from the popular HSE family, can be further increased by optimizing the value for the truncation threshold T_q, beyond the default prescription of $T_q = 2T_g$ of global hybrid functionals.

Work is under way to generalize the implementation by alleviating its dependence on overlap thresholds, to enable calculations of new properties and with more complex exchange-correlation functionals.

ACKNOWLEDGMENTS

The authors acknowledge support from Fondazione ICSC "Italian Research Center on High-Performance Computing, Big Data and Quantum Computing" Spoke 7, Materials and Molecular Sciences—National Recovery and Resilience Plan (PNRR), funded by MUR Missione 4, Componente 2, Investimento 1.4, Next Generation EU (NGEU). This research has received funding from the Project CH4.0 under the MUR program "Dipartimenti di Eccellenza 2023-2027" (CUP Grant No. D13C22003520001).

DATA AVAILABILITY

The data that support the findings of this article are not publicly available upon publication because it is not technically feasible and/or the cost of preparing, depositing, and hosting the data would be prohibitive within the terms of this research project. The data are available from the authors upon reasonable request.

[1] P. Hohenberg and W. Kohn, Inhomogeneous electron gas, Phys. Rev. **136**, B864 (1964).

[2] A. D. Becke, Density-functional thermochemistry. III. The role of exact exchange, J. Chem. Phys. **98**, 5648 (1993).

[3] C. Lee, W. Yang, and R. G. Parr, Development of the Colle-Salvetti correlation-energy formula into a functional of the electron density, Phys. Rev. B **37**, 785 (1988).

[4] J. P. Perdew and Y. Wang, Accurate and simple analytic representation of the electron-gas correlation energy, Phys. Rev. B **45**, 13244 (1992).

[5] C. Adamo and V. Barone, Toward reliable density functional methods without adjustable parameters: The PBE0 model, J. Chem. Phys. **110**, 6158 (1999).

[6] D. I. Bilc, R. Orlando, R. Shaltaf, G.-M. Rignanese, J. Íñiguez, and P. Ghosez, Hybrid exchange-correlation functional for accurate prediction of the electronic and structural properties of ferroelectric oxides, Phys. Rev. B **77**, 165107 (2008).

[7] A. Alkauskas, P. Broqvist, and A. Pasquarello, Defect levels through hybrid density functionals: Insights and applications, Phys. Status Solidi B **248**, 775 (2011).

[8] M. A. L. Marques, J. Vidal, M. J. T. Oliveira, L. Reining, and S. Botti, Density-based mixing parameter for hybrid functionals, Phys. Rev. B **83**, 035119 (2011).

[9] J. Conesa, Modeling with hybrid density functional theory the electronic band alignment at the zinc oxide–anatase interface, J. Phys. Chem. C **116**, 18884 (2012).

[10] J. E. Moussa, P. A. Schultz, and J. R. Chelikowsky, Analysis of the Heyd-Scuseria-Ernzerhof density functional parameter space, J. Chem. Phys. **136**, 204117 (2012).

[11] T. Shimazaki and T. Nakajima, Dielectric-dependent screened Hartree–Fock exchange potential and Slater-formula with Coulomb-hole interaction for energy band structure calculations, J. Chem. Phys. **141**, 114109 (2014).

[12] Z. H. Yang, F. Sottile, and C. A. Ullrich, Simple screened exact-exchange approach for excitonic properties in solids, Phys. Rev. B **92**, 035202 (2015).

[13] D. Koller, P. Blaha, and F. Tran, Hybrid functionals for solids with an optimized Hartree–Fock mixing parameter, J. Phys.: Condens. Matter **25**, 435503 (2013).

[14] J. H. Skone, M. Govoni, and G. Galli, Self-consistent hybrid functional for condensed systems, Phys. Rev. B **89**, 195112 (2014).

[15] A. Erba, Self-consistent hybrid functionals for solids: A fully-automated implementation, J. Phys.: Condens. Matter **29**, 314001 (2017).

[16] A. Savin and H.-J. Flad, Density functionals for the Yukawa electron-electron interaction, Int. J. Quantum Chem. **56**, 327 (1995).

[17] T. Leininger, H. Stoll, H.-J. Werner, and A. Savin, Combining long-range configuration interaction with short-range density functionals, Chem. Phys. Lett. **275**, 151 (1997).

[18] J. Toulouse, F. Colonna, and A. Savin, Long-range–short-range separation of the electron-electron interaction in density-functional theory, Phys. Rev. A **70**, 062505 (2004).

[19] J. Heyd, G. E. Scuseria, and M. Ernzerhof, Hybrid functionals based on a screened Coulomb potential, J. Chem. Phys. **118**, 8207 (2003).

[20] J. Heyd and G. E. Scuseria, Efficient hybrid density functional calculations in solids: Assessment of the Heyd–Scuseria–Ernzerhof screened Coulomb hybrid functional, J. Chem. Phys. **121**, 1187 (2004).

[21] S. Kümmel and L. Kronik, Orbital-dependent density functionals: Theory and applications, Rev. Mod. Phys. **80**, 3 (2008).

[22] N. Kaltsoyannis, J. McGrady, F. Corà, M. Alfredsson, G. Mallia, D. S. Middlemiss, W. C. Mackrodt, R. Dovesi, and R. Orlando, *Principles and Applications of Density Functional Theory in Inorganic Chemistry II* (Springer Science & Business Media, 2004), p. 171.

[23] T. M. Henderson, J. Paier, and G. E. Scuseria, Accurate treatment of solids with the HSE screened hybrid, Phys. Status Solidi B **248**, 767 (2011).

[24] L. Schimka, J. Harl, and G. Kresse, Improved hybrid functional for solids: The HSEsol functional, J. Chem. Phys. **134**, 024116 (2011).

[25] J. Paier, M. Marsman, K. Hummer, G. Kresse, I. C. Gerber, and J. G. Ángyán, Screened hybrid density functionals applied to solids, J. Chem. Phys. **124**, 154709 (2006).

[26] H. Xiao, J. Tahir-Kheli, and W. A. Goddard, III, Accurate band gaps for semiconductors from density functional theory, J. Phys. Chem. Lett. **2**, 212 (2011).

[27] J. M. Crowley, J. Tahir-Kheli, and W. A. Goddard, III, Resolution of the band gap prediction problem for materials design, J. Phys. Chem. Lett. **7**, 1198 (2016).

[28] Z.-Y. Chen and J.-L. Yang, The B3LYP hybrid density functional study on solids, Front. Phys. China **1**, 339 (2006).

[29] K. E. El-Kelany, C. Ravoux, J. K. Desmarais, P. Cortona, Y. Pan, J. S. Tse, and A. Erba, Spin localization, magnetic ordering, and electronic properties of strongly correlated Ln_2O_3 sesquioxides (Ln = La, Ce, Pr, Nd), Phys. Rev. B **97**, 245118 (2018).

[30] J. K. Desmarais, J.-P. Flament, and A. Erba, Fundamental role of Fock exchange in relativistic density functional theory, J. Phys. Chem. Lett. **10**, 3580 (2019).

[31] A. Rettig, J. Lee, and M. Head-Gordon, Even faster exact exchange for solids via tensor hypercontraction, J. Chem. Theory Comput. **19**, 5773 (2023).

[32] C. Pisani and R. Dovesi, Exact-exchange Hartree–Fock calculations for periodic systems. I. Illustration of the method, Intl. J. Quantum Chem. **17**, 501 (1980).

[33] R. Dovesi, C. Pisani, F. Ricca, and C. Roetti, Exact-exchange Hartree-Fock calculations for periodic systems. III. Ground-state properties of diamond, Phys. Rev. B **22**, 5936 (1980).

[34] S. Kokott, F. Merz, Y. Yao, C. Carbogno, M. Rossi, V. Havu, M. Rampp, M. Scheffler, and V. Blum, Efficient all-electron hybrid density functionals for atomistic simulations beyond 10 000 atoms, J. Chem. Phys. **161**, 024112 (2024).

[35] J. K. Desmarais, A. Erba, and R. Dovesi, Generalization of the periodic LCAO approach in the CRYSTAL code to g-type orbitals, Theor. Chem. Acc. **137**, 28 (2018).

[36] V. Saunders, *Methods in Computational Molecular Physics* (Springer, New York, 1983), pp. 1–36.

[37] T. Scott, M. Monagan, I. Grant, and V. Saunders, Numerical computation of molecular integrals via optimized (vectorized) FORTRAN code, Nucl. Instrum. Methods Phys. Res. Sect. A **389**, 117 (1997).

[38] M. García-Blázquez and J. J. Palacios, First-principles excitons in periodic systems with Gaussian density fitting and Ewald potential functions, Phys. Rev. Res. **7**, 013156 (2025).

[39] V. Saunders, C. Freyria-Fava, R. Dovesi, L. Salasco, and C. Roetti, On the electrostatic potential in crystalline systems where the charge density is expanded in Gaussian functions, Mol. Phys. **77**, 629 (1992).

[40] C. Pisani, R. Dovesi, and C. Roetti, *Hartree-Fock Ab initio Treatment of Crystalline Solids*, Lecture Notes in Chemistry Series Vol. 48 (Springer-Verlag, Berlin, 1988).

[41] S. W. de Leeuw, J. W. Perram, and E. R. Smith, Simulation of electrostatic systems in periodic boundary conditions. I. Lattice sums and dielectric constants, Proc. R. Soc. London **373**, 27 (1980).

[42] C. Ribaldone and J. K. Desmarais, Model density approach to Ewald summations, arXiv:2601.21776 .

[43] A. Seidl, A. Görling, P. Vogl, J. A. Majewski, and M. Levy, Generalized Kohn-Sham schemes and the band-gap problem, Phys. Rev. B **53**, 3764 (1996).

[44] R. Garrick, A. Natan, T. Gould, and L. Kronik, Exact generalized Kohn-Sham theory for hybrid functionals, Phys. Rev. X **10**, 021040 (2020).

[45] J. K. Desmarais, G. Ambrogio, G. Vignale, A. Erba, and S. Pittalis, Generalized Kohn-Sham approach for the electronic band structure of spin-orbit coupled materials, Phys. Rev. Mater. **8**, 013802 (2024).

[46] W. Kohn, Image of the Fermi surface in the vibration spectrum of a metal, Phys. Rev. Lett. **2**, 393 (1959).

[47] J. Des Cloizeaux, Energy bands and projection operators in a crystal: Analytic and asymptotic properties, Phys. Rev. **135**, A685 (1964).

[48] S. Ismail-Beigi and T. A. Arias, Locality of the density matrix in metals, semiconductors, and insulators, Phys. Rev. Lett. **82**, 2127 (1999).

[49] L. He and D. Vanderbilt, Exponential decay properties of Wannier functions and related quantities, Phys. Rev. Lett. **86**, 5341 (2001).

[50] R. Resta, Kohn's theory of the insulating state: A quantum-chemistry viewpoint, J. Chem. Phys. **124**, 104104 (2006).

[51] M. Tosi, in *Solid State Physics*, edited F. Seitz and D. Turnbull (Academic Press, New York, 1964), Vol. 16, p. 1.

[52] W. Jones and N. H. March, *Theoretical Solid State Physics* (Courier Corporation, 1985), Vol. 35.

[53] B. Carlson and G. Rushbrooke, in *Mathematical Proceedings of the Cambridge Philosophical Society* (Cambridge University Press, Cambridge, 1950), Vol. 46, pp. 626–633.

[54] R. J. Buehler and J. O. Hirschfelder, Bipolar expansion of Coulombic potentials, Phys. Rev. **83**, 628 (1951).

[55] B. Bayman, A generalization of the spherical harmonic gradient formula, J. Math. Phys. **19**, 2558 (1978).

[56] A. Erba, J. K. Desmarais, S. Casassa, B. Civalleri, L. Doná, I. J. Bush, B. Searle, L. Maschio, L. Edith-Daga, A. Cossard, *et al.*, CRYSTAL23: A program for computational solid state physics and chemistry, J. Chem. Theory Comput. **19**, 6891 (2023).

[57] See Supplemental Material at http://link.aps.org/supplemental/10.1103/wgd9-321t for a description of the adopted basis sets

and Monkhorst-Pack meshes, input decks, and a breakdown of total timings into various computational tasks.

[58] J. P. Perdew, K. Burke, and M. Ernzerhof, Generalized gradient approximation made simple, Phys. Rev. Lett. **77**, 3865 (1996).

[59] F. Pascale, M. Pastore, K. Doll, and R. Dovesi, On the role of the exact Hartree–Fock exchange in determining the Jahn–Teller energy splitting and electronic band gap in the KBF3 (B = Sc, Ti, Fe, Co, Cr and Cu) perovskites. A quantum mechanical investigation, Chem. Phys. Lett. **836**, 141053 (2024).

[60] B. Civalleri, P. D'Arco, R. Orlando, V. Saunders, and R. Dovesi, Hartree–Fock geometry optimisation of periodic systems with the Crystal code, Chem. Phys. Lett. **348**, 131 (2001).

[61] K. Doll, Analytical stress tensor and pressure calculations with the CRYSTAL code, Mol. Phys. **108**, 223 (2010).

[62] A. Erba, A. Mahmoud, D. Belmonte, and R. Dovesi, High pressure elastic properties of minerals from *ab initio* simulations: The case of pyrope, grossular and andradite silicate garnets, J. Chem. Phys. **140**, 124703 (2014).

[63] R. Dovesi, R. Orlando, B. Civalleri, C. Roetti, V. R. Saunders, and C. M. Zicovich-Wilson, CRYSTAL: A computational tool for the *ab initio* study of the electronic properties of crystals, Z. Kristallogr. **220**, 571 (2005).

[64] S. Casassa, A. Erba, J. Baima, and R. Orlando, Electron density analysis of large (molecular and periodic) systems: A parallel implementation, J. Comput. Chem. **36**, 1940 (2015).

[65] A. Erba, J. Baima, I. Bush, R. Orlando, and R. Dovesi, Large-scale condensed matter DFT simulations: Performance and capabilities of the CRYSTAL code, J. Chem. Theory Comput. **13**, 5019 (2017).

[66] G. Ambrogio, L. Donà, J. K. Desmarais, C. Ribaldone, S. Casassa, F. Spiga, B. Civalleri, and A. Erba, Accelerated linear algebra for large scale DFT calculations of materials on CPU/GPU architectures with CRYSTAL, J. Chem. Phys. **162**, 082501 (2025).

[67] J. K. Desmarais, J.-P. Flament, and A. Erba, Spin-orbit coupling from a two-component self-consistent approach. II. Non-collinear density functional theories, J. Chem. Phys. **151**, 074108 (2019).

[68] J. K. Desmarais, A. Erba, and J.-P. Flament, Structural relaxation of materials with spin-orbit coupling: Analytical forces in spin-current DFT, Phys. Rev. B **108**, 134108 (2023).

[69] J. K. Desmarais, J.-P. Flament, and A. Erba, Spin-orbit coupling in periodic systems with broken time-reversal symmetry: Formal and computational aspects, Phys. Rev. B **101**, 235142 (2020).

[70] J. K. Desmarais, J.-P. Flament, and A. Erba, Adiabatic connection in spin-current density functional theory, Phys. Rev. B **102**, 235118 (2020).

[71] J. K. Desmarais, S. Komorovsky, J.-P. Flament, and A. Erba, Spin–orbit coupling from a two-component self-consistent approach. II. Non-collinear density functional theories, J. Chem. Phys. **154**, 204110 (2021).

[72] J. K. Desmarais, J. Maul, B. Civalleri, A. Erba, G. Vignale, and S. Pittalis, Spin currents via the gauge principle for meta-generalized gradient exchange-correlation functionals, Phys. Rev. Lett. **132**, 256401 (2024).

[73] J. K. Desmarais, G. Vignale, K. Bencheikh, A. Erba, and S. Pittalis, Electron localization function for noncollinear spins, Phys. Rev. Lett. **133**, 136401 (2024).

[74] A. Boccuni, B. M. T. C. Peluzo, F. Bodo, G. Ambrogio, J. Maul, D. Mitoli, G. Vignale, S. Pittalis, E. Kraka, J. K. Desmarais, *et al.*, Unveiling the role of spin currents on the giant Rashba splitting in single-layer WSe_2, J. Phys. Chem. Lett. **15**, 7442 (2024).

[75] J. K. Desmarais, A. Erba, Y. Pan, B. Civalleri, and J. S. Tse, Mechanisms for pressure-induced isostructural phase transitions in EuO, Phys. Rev. Lett. **126**, 196404 (2021).

[76] S. Onari, T. Arai, and K. Kudo, Infrared lattice vibrations and dielectric dispersion in α-Fe_2O_3, Phys. Rev. B **16**, 1717 (1977).

[77] P. Liao and E. A. Carter, Testing variations of the GW approximation on strongly correlated transition metal oxides: Hematite (α-Fe_2O_3) as a benchmark, Phys. Chem. Chem. Phys. **13**, 15189 (2011).

[78] S. Piccinin, The band structure and optical absorption of hematite (α-Fe_2O_3): A first-principles GW-BSE study, Phys. Chem. Chem. Phys. **21**, 2957 (2019).

[79] F. Tran and P. Blaha, Importance of the kinetic energy density for band gap calculations in solids with density functional theory, J. Phys. Chem. A **121**, 3318 (2017).

[80] D. Le, A. Barinov, E. Preciado, M. Isarraraz, I. Tanabe, T. Komesu, C. Troha, L. Bartels, T. S. Rahman, and P. A. Dowben, Spin–orbit coupling in the band structure of monolayer WSe_2, J. Phys.: Condens. Matter **27**, 182201 (2015).

[81] C. Zhang, Y. Chen, A. Johnson, M.-Y. Li, L.-J. Li, P. C. Mende, R. M. Feenstra, and C.-K. Shih, Probing critical point energies of transition metal dichalcogenides: Surprising indirect gap of single layer WSe_2, Nano Lett. **15**, 6494 (2015).

[82] K. Kośmider, J. W. González, and J. Fernández-Rossier, Large spin splitting in the conduction band of transition metal dichalcogenide monolayers, Phys. Rev. B **88**, 245436 (2013).

[83] Z. Zhu, Y. Cheng, and U. Schwingenschlögl, Giant spin-orbit-induced spin splitting in two-dimensional transition-metal dichalcogenide semiconductors, Phys. Rev. B **84**, 153402 (2011).

[84] A. Kormányos, G. Burkard, M. Gmitra, J. Fabian, V. Zólyomi, N. D. Drummond, and V. Fal'ko, $\mathbf{k}\cdot\mathbf{p}$ theory for two-dimensional transition metal dichalcogenide semiconductors, 2D Mater. **2**, 022001 (2015).

[85] J. Kang, S. Tongay, J. Zhou, J. Li, and J. Wu, Band offsets and heterostructures of two-dimensional semiconductors, Appl. Phys. Lett. **102**, 012111 (2013).

[86] H. Miyazaki, T. Ito, H. J. Im, S. Yagi, M. Kato, K. Soda, and S. Kimura, Direct observation of momentum-dependent exchange interaction in a Heisenberg ferromagnet, Phys. Rev. Lett. **102**, 227203 (2009).

[87] N. M. Souza-Neto, J. Zhao, E. E. Alp, G. Shen, S. V. Sinogeikin, G. Lapertot, and D. Haskel, Reentrant valence transition in EuO at high pressures: Beyond the bond-valence model, Phys. Rev. Lett. **109**, 026403 (2012).

[88] S. Stavrić, G. Cuono, B. Yang, Á. R. Puente-Uriona, J. Ibañez-Azpiroz, P. Barone, A. Droghetti, and S. Picozzi, Giant nonreciprocal band structure effect in a multiferroic material, Phys. Rev. Lett. **135**, 206401 (2025).